City Research Online

City, University of London Institutional Repository

Performance and Loss Analysis of Squirrel Cage Induction Machine Based Flywheel Energy Storage System

Abid Soomro *, Mustafa E. Amiryar[ID], Daniel Nankoo and Keith R. Pullen[ID]

School of Mathematics, Computer Science and Engineering, University of London, London EC1V 0HB, UK;
mustafa.amiryar.2@city.ac.uk (M.E.A.); d.nankoo@city.ac.uk (D.N.); k.pullen@city.ac.uk (K.R.P.)

* Correspondence: abid.soomro.1@city.ac.uk; Tel.: +44-(0)20-7040-3475

Abstract: Flywheel energy storage systems (FESS) are one of the earliest forms of energy storage technologies with several benefits of long service time, high power density, low maintenance, and insensitivity to environmental conditions being important areas of research in recent years. This paper focusses on the electrical machine and power electronics, an important part of a flywheel system, the electrical machine rotating with the flywheel inertia in order to perform charge-discharge cycles. The type of machine used in the electrical drive plays an important role in the characteristics governing electrical losses as well as standby losses. Permanent magnet synchronous machine (PMSM) and induction machines (IM) are the two most common types of electric machines used in FESS applications where the latter has negligible standby losses due to its lower rotor magnetic field until energised by the stator. This paper describes research in which the operational and standby losses of a squirrel-cage induction machine-based flywheel storage system (SCIM-FESS) are modelled as a system developed in MATLAB/Simulink environment inclusive of the control system for the power electronics converters. Using the proposed control algorithm and in-depth analysis of the system losses, a detailed assessment of the dynamic performance of the SCIM-FESS is performed for different states of charging, discharging, and standby modes. The results of the analysis show that, in presence of system losses including aerodynamic and bearing friction losses, the SCIM-FESS has satisfactory characteristics in energy regulation and dynamic response during load torque variations. The compliance of FESS and its conversion between the generating and motoring mode within milliseconds show the responsiveness of the proposed control system.

Keywords: flywheel energy storage; squirrel cage induction machine; loss analysis; field-oriented control

1. Introduction

Cleaner production of energy is urgently needed in today's world due to the concerns about global warming and growing population. This need has allowed widespread use of distributed generation (DG) and renewable energy sources (RES) integrated to electricity networks [1]. However, due to their dependency on seasonal variations, RES are not completely reliable and stable and cannot be used as the only primary source of energy. Additionally, if renewable sources of energy are added into microgrids powered previously only by fossil fired engines, this intermittency combined with fluctuation in demand leads to further stability challenges. Energy storage systems (ESS) offer a solution, which can mitigate the effects of RES intermittency by providing a balance between electrical supply and demand [2,3]. ESS can also reduce the power rating of the generating engine to meet peak demand and enables power production to meet average demand and reducing generation cost [4]. Also,

there are various solutions proposed to ensure network stability and reliability with RES including demand management, interconnection with external grids, and ESS [5].

There are ranges of systems involved in energy storage process, which can convert, store and deliver energy on demand. Performance of these systems depends on the amount of energy they can store, the storage time and delivery of energy with minimum losses [6]. Therefore, high power capability, high efficiency, low capital cost and environmentally friendly attributes improve the value of ESS [7].

A FESS is an assembly of a rotating mass, electrical machine, power electronics converter, bearing system and containment. The design of the rotor used in FESS depends on the materials from which they are made. Solid disk or solid cylinder are made from isotropic materials like steel. Rim type or hollow cylinder flywheel rotors are constructed from non-isotropic material like composite carbon fiber. Solid disk or solid cylinder flywheel rotors have simple construction and are commonly used [8]. Solid rotor flywheels exhibit less displacement from axes due to centrifugal forces hence simplifying flywheel attachment to the shaft and with electrical machine [9]. Schematic diagram of solid rotor FESS is shown in Figure 1.
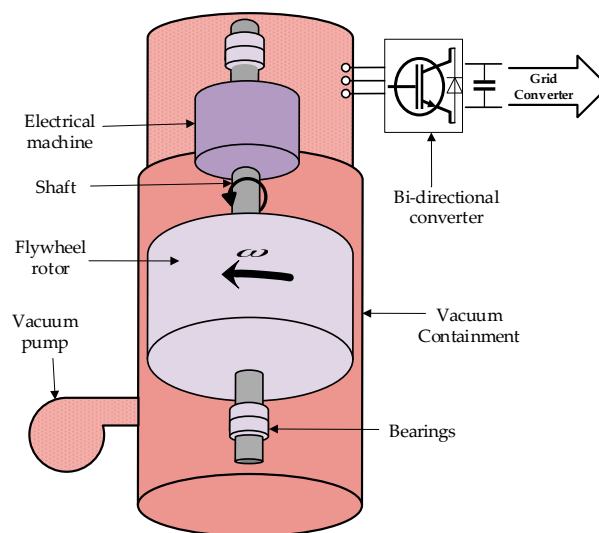
Figure 1. Structure of solid disk FESS.

Carbon fibre-reinforced composite rim type or hollow cylinder flywheel rotor assembly contains the hub and the flywheel rim, which are mounted together on the metallic shaft [10]. Due to mismatching of strains of hub and the flywheel rim material, attachment of the composite flywheel to the shaft is an issue, due to this issue, integrated hollow flywheel design is introduced recently, in which electric machine and bearing system are integrated in the hub of the flywheel [11]. In this design, the rotor of electric machine is outside of the stator which enables very high-speed design [9]. Integrated hollow flywheels attain high speeds, have more specific energy, less cost, occupy less space and contain less windage losses. However, shaftless hollow flywheel design faces challenges such as heating issues, strength of the rotor materials and suspension of the rotor [9,11]. Schematic diagram of integrated hollow flywheel is shown in Figure 2. This configuration holds an axial type PMSM with two PM rotors and a single stator. In addition, there are some other configurations including the type in which the flywheel and the rotor of the electric machine are combined together as addressed in [12].
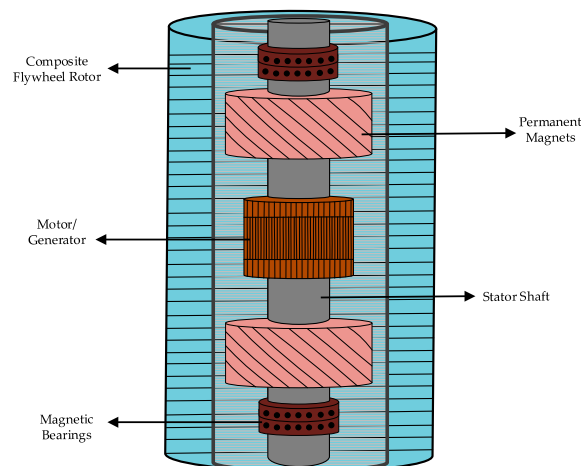
Figure 2. Structure of Integrated hollow FESS.

With fast response time, relatively high-energy density and high-power capability, flywheel energy storage systems (FESS) offer an attractive energy storage solution [13]. FESS is highly suitable for applications where a large number of daily charge-discharge cycles as required for power smoothing, renewable energy integration, stability and power quality improvement [14]. FESS and battery energy storage systems (BESS) can be strong competitors against each other for a number of applications [15], with FESS being best suited and leading the competition for short term and high-power applications. Unlike FESS, performance of BESS is affected by many factors and importantly the temperature dependency [15]. Hence, the BESS is less favorable in countries where temperatures are high throughout the year. BESS cannot withstand high charge-discharge rates and requires quite a large volume to store a larger amount of energy [16]. Moreover, the research findings in [17] show that the probability of a battery storage failure is seven times more likely than that of a flywheel storage which makes BESS less reliable than FESS. However, costs of BESS have reduced significantly in recent years and have the added advantage of durations of around one to two hours so may provide power for longer periods. On the other hand, the cost of flywheels needs to reduce significantly and this is possible with lower cost design and volume manufacture [18].

Recently, FESS technology has been implemented in many applications such as UPS, aerospace, transport, power levelling, wind power and frequency regulations. FESS has been successfully used to secure critical loads during power outages in the microgrid environment [17]. In [19], a low speed FESS has been used as a hybrid UPS composed of an engine generator and a flywheel to improve voltage fluctuations of less than 2%. To support emergency loads when main grid supply is disconnected, a successful utilisation of a FESS used as a UPS instead of BESS is reported in [20]. As an alternative to batteries, the flywheel technology has been used for removing DC voltage ripples [21], short-term ride through [22], fast balancing of power in microgrids [23], and islanded solar PV systems [24].

The electrical machine is a key part of a FESS which performs the charge-discharge cycles and can be responsible for major losses in the process. The choice of electrical machine must be carefully made according to the application requirements. Machines commonly used in FESS are induction machines (IM), permanent magnet synchronous machines (PMSM), switched reluctance machines (SRM) and homopolar synchronous machines (HSM). SRM have robust design, fault tolerant capability and ability to operate in high temperature environments; however, it is less commonly used because of its complex torque current and high current ripples [25]. Due to the use of electromagnets, SRM can be completely demagnetised [6] that would lead to no idling losses at zero torque (no load) [26]. Highly nonlinear behavior of SRM makes selection of suitable control gains difficult and this makes design of control system challenging and problematic [27]. In the generator mode, SRM require excitation to produce power [25] produced by means of electronic converter [28], but it will result in extra losses. PMSM is used in high-speed applications due to its very high efficiency while the IM,

due to its rugged construction, is used for high power applications [29]. A challenge for IM is the mechanical design in high-speed application, which can be overcome by using appropriate solid-rotor topologies such as slotted solid rotor, coated solid rotor, caged solid rotor and smooth solid rotor [25]. Homopolar synchronous machines (HSM) are used for long-term energy storage in high speed and high efficiency applications. HSM have robust rotor design and due to their lower standby losses compared to PMSM, they can be used an alternative to PMSM in high-speed applications [25,30]. However, the main disadvantage is the difficult design of HSM due to its complex magnetic flux paths and geometry [31].

Many researchers have studied induction machine-based FESS, but a thorough analysis of the performance of IM in FESS is lacking [32–36]. An IM-based FESS and its associated control strategies for wind energy system applications is presented in [37] and performance analysis of an IM-FESS for use as a UPS for compensation of momentary voltage drops is discussed in [38]. However, analysis of the IM losses as well as the methods for determination of flywheel idling losses is neglected in both papers. Authors in [39] discuss the model and control of an induction machine for flywheel applications focusing on frequency regulation, however, the dynamic performance of the IM and analysis of the control system is lacking. The research in [40] discusses a simple flywheel storage system for DC microgrid proposing an open loop volt/hertz control system governing the energy flow of the FESS. However, the volt/hertz control system is inefficient to achieve high performance [41] since the FESS is a dynamic system and needs efficient control system to achieve dynamic stability and fast flow of the energy.

In this paper, a model for an induction machine driven flywheel storage system has been developed and described with detailed simulation results presented. A detailed loss analysis of the IM has been studied and embedded in the model as developed in MATLAB/Simulink. In addition, the performance of the machine is analysed for motoring and generating modes controlling the charge-discharge cycles of the flywheel storage. Following the introduction, a brief background of the flywheel history along with its theory and structure are described in Section 2. The loss analysis of the system as described including standby losses and operational losses are studied in Section 3. A detailed analysis of the proposed control strategies and development of the model of IM driven flywheel system is presented in Section 4. The analysis of results is presented in Section 5. The results are discussed and conclusion is made in Section 6.

2. Flywheel Theory and Structure

2.1. Background

FESS is a device with a rotating mass that can maintain its inertia to store energy in the form of kinetic storage. Flywheels are one of the early forms of mechanical storage systems in history and were first used in boats, steam engines and trains during the industrial revolution in the 18th century [42]. During the 1950s flywheels were used to build gyro buses [43], first generation FESS comprised of a large steel wheel attached to an axle. After advancement in materials in 1970s, the light and high tensile strength carbon composite rotors were used in FESS [44]. Successful research and advancement in magnetic materials, magnetic bearings and modern power electronics have made it possible for flywheel technology to compete with other energy storage systems and specifically with electro chemical batteries and super capacitors [45]. A modern steel rotor flywheel with a weight of 1t can run at peripheral speed of 500 m/s compared to the flywheels used in stationary steam engines during the industrial age, which could barely exceed the peripheral speed of 20 m/s, modern flywheels can store up to 25 kWh of useable energy when compared to the industrial age flywheels that weighed 50 tons and could store 5 kWh of energy [8]. Modern flywheels can achieve high round trip efficiency of more than 90% with frictional losses of less than 3% of energy per hour and lifetime of over 20 years with high power and energy density, if a low-pressure vacuum is maintained, carbon fiber flywheels can reach up to rotational speeds of 100,000 RPM [46,47]. It can be used as a power buffer to considerably

reduce peak currents drawn from any other storage system such as BESS that results in improving life of the battery [13]. Flywheel technology can replace battery systems in aerospace applications as it has been found that FESS would be 35% lighter and 55% smaller compared to BESS for EOS-AMI type spacecraft [48]. Flywheels are commonly used for ride through applications mainly to improve power quality. Flywheels have also been used for voltage regulation [34] and spinning reserves for sensitive loads in data centers [17]. They are integrated to solar photovoltaic (PV) system for load levelling [49], harmonic compensation [35], high power UPS system for plasma experiments [50], and in the distribution network to improve power reliability [36].

2.2. Components of FESS

A flywheel storage system works in three modes of acceleration, standby and deceleration. The structure of FESS consists of a bearing system, motor/generator set, flywheel rotor, power electronics and a low-pressure vacuum containment. All these components together determine the overall efficiency of the FESS and are briefly described in this section.

2.2.1. Flywheel Rotor

The rotor of the flywheel is a rotating mass m (kg) with inertia J (kg·m^2) that spins at an angular velocity of ω (rad/s) and stores kinetic energy E (joules) as given by Equation (1).

$$E = \frac{1}{2} J \omega^2 \tag{1}$$

The useable stored kinetic energy of a flywheel spinning between a minimum and maximum velocity of ω is given by:

$$E = \frac{1}{2} J (\omega_{max}^2 - \omega_{min}^2) \tag{2}$$

where the moment of inertia J is a function of flywheel geometry and mass. In case of a disc type flywheel with mass m (kg), density ρ (kg/m^3) and length l (m), the angular velocity can be expressed by Equation (3):

$$\omega = \frac{2}{r} \sqrt{\frac{E}{\rho \pi l}} \tag{3}$$

Therefore, the stored energy is expressed by Equation (4) [51].

$$E = \frac{1}{4} m r^2 (\omega_{max}^2 - \omega_{min}^2) \tag{4}$$

In the case of a cylindrical type flywheel with an inner radius r_1 and outer radius r_2, the stored kinetic energy is given by Equation (5).

$$E = \frac{1}{4} m (\omega_{max}^2 - \omega_{min}^2)\left(r_2^2 - r_1^2\right) \tag{5}$$

2.2.2. Electric Machines

The electrical machine is coupled with the flywheel and acts as a motor to accelerate and charge the flywheel transforming electrical energy into kinetic energy when positive torque is applied on the mechanical shaft. The same machine can function as a generator to decelerate and discharge the flywheel to transform kinetic energy into electrical energy with a negative torque. Desirable features for an electrical machine to be used in FESS are high efficiency, low standby losses and low cost. Advantages and drawbacks of commonly used electrical machines in FESS are presented in Table 1.

Table 1. Advantages and drawbacks of commonly used electrical machines in FESS [13,25,47,52,53].

	SCIM	PMSM	SRM
Advantages	Rugged construction	Simple rotor design	Robust simple structure
	No risk of demagnetization	High power, high load and high torque density	High power density
	Low cost	Easy to install and maintain due to smaller size	Low cost
	High efficiency (93.4%)	Very high efficiency (95.5%)	High efficiency (93%)
	No idling losses due to its lower rotor magnetic field at zero torque value, consequently this reduces a total electrical loss of IM	No field winding losses due to use of permanent magnets	No idling losses
	High torque and high power capability	Suitable to operate in low pressure vacuum with negligible rotor losses	Wide speed range
Drawbacks	Difficult mechanical design for high speed applications	Risk of sudden demagnetization	Significant rotor eddy current losses due to the time varying magnetic field
	Difficult to operate in absolute vacuum due to complex heat transfer system	Due to use of permanent magnets, PMSM have low tensile strength	High torque and current ripples
	Limited speed and larger volume	High cost	Difficult to regulate speed
	Copper losses in electromagnets during field excitation due to high inrush currents	Idling losses at zero torque due to presence of magnetic field	High losses due to need of excitation

2.2.3. Bearing Systems

The bearing system supports the rotor and allows the flywheel to spin freely. The selection of bearing system depends on many factors but importantly on its lifetime, weight and level of acceptable losses [54]. There are two types of bearings commonly used in FESS: (1) mechanical bearings and (2) magnetic bearings. Mechanical bearings are simple in structure but have major losses due to friction and deterioration of lubricants and they require maintenance such as lubrication replacement. Magnetic bearing systems work using magnetic levitation and do not have any contact with the mechanical shaft of the flywheel. They are stable but low loss bearing systems due to less friction and are suitable for high-speed applications in FESS [55]. Magnetic bearings that use permanent magnets for levitation are called passive magnetic bearings whereas active bearings are the type that make use of a feedback system with electrical coils [56]. Active magnetic bearings require continuous power for energisation of the magnetic levitation system [13].

The combined use of magnetic and mechanical bearing in FESS can make the system more stable, cost effective and less complex; an example of such system is discussed in [57]. Another type of bearing called spiral groove bearing (SGB) is low loss bearing system, used for low speed applications of less than 10 m/s. SGB is used in combination with magnetic bearing for flywheels with larger storage capacity and less frequency vibrations of the rotor [58]. A technique has been developed by Argonne National Laboratory to produce high-temperature superconducting (HTS) bearing system to reduce

rotational losses to less than 2% per day of stored energy. Compared to magnetic and mechanical bearing, HTS bearings incur half of the rotational loss of conventional mechanical bearings [59].

2.2.4. Power Electronics Interface

The electrical machine is connected to a power electronics converter interface in order to make power flow from the electrical grid to the FESS and back to the grid during the acceleration and deceleration of the flywheel. Bi-directional converters help exchange power between the grid and FESS by controlling the operation of the electrical machine. The power electronics converter, which is near to electrical machine, controls rotor magnetic flux and speed of the electrical machine with a suitable modulation technique to produce the gate pulses for the converter. An AC-DC converter (grid side converter) with suitable modulation technique is used to maintain a constant DC-link voltage by following grid side reference currents to control flow of active and reactive power [14]. The design of the converter and its switching technique are responsible for the power quality of the system considering that nearly sinusoidal stator currents, low total harmonic distortion THD (less than 5%) and stable DC-link voltage are the factors affecting the power quality in FESS [60]. The combination of AC-DC-AC power converters is called the back-to-back (BTB) configuration and is the most widely used topology in FESS applications [53]. Oliveira in [61] has discussed implementation and control of AC-DC-AC in FESS. A new DC-DC boost inverter topology used for low speed flywheels is proposed in [62]. Different topologies of power electronics converters used in FESS are discussed in details in [25].

2.2.5. Containment

The flywheel rotor must be enclosed in containment casing for the purpose of safety and reducing aerodynamic losses. The containment could prevent collateral damage which can happen due to the bearing failure releasing the rotor or rotor failure itself or growth of a crack in case of solid steel rotor flywheel. A fatigue crack may grow to cause the rotor to break in large fragments and can cause huge damage to surroundings. In the case of carbon composite flywheel rotors, failure occurs due to circumferential fractures of rotor in layer or propagation of cracks in the rotor. This can cause the rotor to disintegrate into rings or may result into the fragments and powder of carbon fiber that is highly flammable [63]. The rapid disintegration of a composite rotor can also lead to a very high-pressure build up only contained by thick casing or bunkering. In order to increase further safety of solid steel and carbon composite flywheels, they are installed in underground bunkers [46]. This can be eliminated by use of laminated steel designs which greatly limit any rotor failure to small energy release. If the casing is not sufficiently good, horizontal axle FESS has more possibility of mass center displacement than vertical axle FESS that causes instability of the rotor [13]. The aerodynamic losses are reduced by creating a low-pressure environment for the rotor in the containment. Depending on the peripheral speed of the flywheel, containments are made of high strength steel or composite materials [53]. For higher speed flywheels, containment is filled with helium or completely evacuated in order to reduce rotor stress and windage losses, considering that the windage losses are negligible for less than 1 mbar pressure [59].

3. Loss Calculation of IM Driven FESS

There are different losses in a FESS including power converter losses, stator losses and rotor losses all of which fall into the category of electrical losses and contribute to the conversion efficiency. The mechanical losses of the system are mainly due to the bearing losses and aerodynamic or windage losses. The power balance Equation for squirrel cage induction machine FESS (SCIM-FESS) is given by Equation (6).

$$P_{out} = P_{ag} - P_{rcl} - P_{rfe} - P_{mech} \tag{6}$$

where:

$$P_{ag} = P_{in} - P_{scl} - P_{sfe} \tag{7}$$

$$P_{out} = P_{in} - P_{scl} - P_{rcl} - P_{rfe} - P_{sfe} - P_{mech} \tag{8}$$

$$P_{in} = P_{out} + P_{scl} + P_{rcl} + P_{rfe} + P_{sfe} + P_{bearing} + P_{windage} \tag{9}$$

where P_{ag} is the power transferred from stator to rotor of IM across the air-gap, P_{in} is the input power, P_{out} is total output power, P_{scl} is stator copper loss of IM, P_{rcl} is rotor copper loss of IM, P_{rfe} and P_{sfe} are core losses in the rotor and stator, $P_{bearing}$ and $P_{windage}$ are bearing and windage losses of FESS, respectively.

3.1. SCIM-FESS Design and Parameters

In this research, the considered flywheel system is a cylindrical rotor type made of steel laminates and operated in very low-pressure vacuum running between a speed range of 10–20 krpm. The type of bearings used are single row radial ball bearings with micro drip type of lubrication. Table 2 shows the parameters of the electrical machine and other necessary parameters used in SCIM-FESS system design. The detailed calculation and analysis of the switching and conduction losses in power electronics converters are not carried out here but assumed with a fixed value not to exceed more than 2% of the total energy produced in one cycle. This is added to the electrical and mechanical losses when the total system losses are calculated.

Table 2. Values of coefficients and parameters of SCIM-FESS.

Parameter	Value
Stator Resistance (R_s)	11.85 mΩ
Rotor Resistance (R_r)	9.29 mΩ
Stator leakage inductance (L_{ls})	0.2027 mH
Rotor leakage inductance (L_{lr})	0.2027 mH
Mutual Inductance (L_m)	9.295 mH
Rated magnetic flux (λ_m)	0.75 Weber
Power rating	100 kW
Nominal torque	90 N·m
Maximum speed	20 krpm
Minimum speed	10 krpm
Switching frequency	20 kHz
DC bus voltage	600 V
Air density (ρ)	0.0011 kg/m^3
Air dynamic viscosity (μ)	1.91×10^{-5} kg/m·s
Flywheel rotor outer diameter (D_{r0})	0.4 m
Shaft diameter (D_s)	0.025 m
Bearing design factor (f_L)	0.0005
Kinematic oil viscosity (V_0)	130×10^6 m^2/s
Lamination thickness (t)	0.15 mm
Conductivity of electrical steel (σ)	2.08×10^6 Siemens/m
Density of electrical steel (ρ)	7650 kg/m^3

3.2. Electrical Losses

The electrical losses in FESS are mainly the due to the stator and rotor losses in the motor/generator set. The stator electrical losses are the combination of copper losses (P_{scl}) in the stator winding and core losses (P_{core}) in the stator core. The stator copper losses are proportional to the square of the RMS magnitude of stator currents I_s and is dependent on the value of the stator resistance R_s. Core losses (eddy current and hysteresis losses) is the function of electrical angular frequency f_e and maximum

magnetic flux density B_m. Equation (10) presents the general relation of core losses in the electrical machine while the total electrical losses in the stator of IM are given by Equation (11).

$$P_{core} = \left(K_{hys}f_e + K_e f_e^2\right)B_m^2 \tag{10}$$

$$P_{stator} = 3I_s^2 R_s + \left(K_{hys}f_e + K_e f_e^2\right)B_m^2 \tag{11}$$

where K_{hys} is the Steinmetz co-efficient, B_m is peak magnetic flux density and K_e is a constant factor as given by Equation (12) [64].

$$K_e = \frac{\pi^2 t^2 \sigma}{6\rho} \tag{12}$$

where t is the thickness of laminations, σ is electrical conductivity and ρ is the density of the electrical steel.

The rotor copper losses (P_{rcl}) are also a combination of copper and rotor iron losses (P_{core}) and are given by Equation (13).

$$P_{rotor} = 3I_r^2 R_r + \left(K_{hys}f_{sl} + K_e f_{sl}^2\right)B_m^2 \tag{13}$$

where, $f_{sl} = sf_e$, s is the slip, R_r is rotor resistance and I_r is the RMS magnitude of rotor currents in one phase of the rotor.

For calculation of Steinmetz coefficient (K_{hys}), Equation (10) is divided by the term $f_e B_m^2$ to create a linear relationship.

$$\frac{P_{core}}{f_e B^2{}_m} = (x + yf_e) \tag{14}$$

where, $x = K_{hys}$ and $y = K_e$ which can be simply calculated by substituting the values of parameters (t, ρ and σ) into Equation (12) provided in Table 2 giving $y = 3.34 \times 10^{-3}$ Hz. The value of x can be calculated by linear fitting of Equation (14) for the best approximation of the data.

The stator and rotor core of the IM are assumed to be made of electric steel M470-50HP. Manufacturer's core loss data for M470-50HP is shown in Table 3 where the core loss data for specific electrical frequencies of 50 Hz, 100 Hz, 200 Hz and 400 Hz is provided. The electrical frequency of SCIM-FESS presented in this paper at 20 krpm is 333 Hz that lies between 200 Hz and 400 Hz. Therefore, the values of B_m at 333 Hz is approximated between 0.6–0.7 Tesla as calculated based on the methodology discussed in [65].

Table 3. Manufacturer's loss data for M470-50HP electrical steel. Adapted with permission from [66], Cogent Power Inc., 2019.

B_m (T)	W/kg at 50 Hz	W/kg at 100 Hz	W/kg at 200 Hz	W/kg at 400 Hz
0.1	0.03	0.07	0.23	0.58
0.2	0.13	0.29	0.84	2.14
0.3	0.26	0.61	1.71	4.37
0.4	0.43	1.00	2.78	7.17
0.5	0.63	1.46	4.03	10.6
0.6	0.85	1.98	5.48	14.7
0.7	1.09	2.55	7.12	19.6
0.8	1.34	3.19	9.02	25.4
0.9	1.62	3.91	11.2	32.4
1	1.94	4.71	13.7	40.6

Substituting the values of x and y in Equation (14), the relation of P_{core} can be written as:

$$P_{core} = \left(0.0487 f_e + 1.4 \times 10^{-3} f_e\right) \tag{15}$$

Using Equation (15) and substituting the values of resistances into Equations (11) and (13), the total electrical losses of the stator and rotor are given by:

$$P_{stator} = \left(0.099 I_s^2\right) + \left(0.048 f_e + 1.4 \times 10^{-3} f_e\right) \tag{16}$$

$$P_{rotor} = \left(0.027 I_r^2\right) + \left(9.6 \times 10^{-4} f_e + 2.8 \times 10^{-4} f_e\right) \tag{17}$$

3.3. Mechanical Losses

3.3.1. Windage Loss

The windage losses in a FESS are due to the friction between the rotating surfaces and the surrounding medium, which is air in most cases. The windage loss increases with increase of the flywheel speed and is proportional to the cube of the flywheel angular velocity [67]. The windage losses of the FESS housed in a containment for the pressure of >100 Pa is given by Equation (18).

$$P_w = \frac{1}{64} C_m \omega^3 \rho \left(D_{r0}^5 - D_{r1}^5\right) \tag{18}$$

where $C_m = \frac{3.87}{\sqrt{R_e}}$ is the torque coefficient, R_e is the Reynolds number and is given by $R_e = \sqrt{\frac{\rho \omega D_{r0}^2}{4\mu}}$, ρ is the coolant density and μ is the dynamic viscosity of air [3].

For the high-speed rotor flywheels operating in low air pressure environments (0.1 Pa to 10 Pa), windage losses of the FESS is given by Equation (19) [68].

$$P_w = \frac{P}{2} \sqrt{\frac{2\pi}{RT}} \omega^2 a^4 \tag{19}$$

where, P is the gas pressure, a is radius of the rotor disk and R is the gas constant. By substituting values of parameters (R_e and C_m) and coefficients from Table 2 in Equations (18) and (19). The simplified Equations for windage losses can be written as:

$$\begin{cases} P_w = 4.5 \times 10^{-7} \omega^{2.5} & P \geq 100 \\ P_w = 6.6 \times 10^{-6} \omega^2 & P \leq 10 \end{cases} \tag{20}$$

3.3.2. Bearing Losses

The bearing losses are usually calculated using the empirical methods as recommended by the bearing manufacturers. However, due to the complexity of the empirical method, in this paper the bearing power losses are calculated using the analytical method. Considering the rotating contacts, the bearing losses in FESS can be defined by Equation (21) [69].

$$t_b = t_l + t_v + t_f \tag{21}$$

where, t_l is the torque due to an applied load and depends on the type of the load and design of bearing, t_f is end flange friction torque which is only applicable in roller type bearings and is negligible in ball bearings, and t_v is the torque due to viscous friction that is dependent on the speed and property of the lubricant used. The values for t_l and t_v can be calculated using Equations (22) and (23), respectively [70].

$$t_l = f_l F_b D_p \tag{22}$$

$$\left. \begin{array}{ll} t_v = 10^{-7} f_0 (v_0 n)^{\frac{2}{3}} D_p^3 & v_0 n \geq 2000 \\ t_v = 160 \times 10^{-7} f_0 (v_0 n)^{\frac{2}{3}} D_p^3 & v_0 n < 2000 \end{array} \right\} \tag{23}$$

where f_l is the design dependent factor and is defined by Equation (24).

$$f_l = z \left(\frac{F_s}{C_s} \right)^y \tag{24}$$

where C_s is static load rating defined by the manufacturer's datasheets and F_s the static equivalent load. The values of z and y depend on the type and contact angle of the bearing as given in Table 4. F_b is load on the bearing, D_p is the pitch circle diameter (m), n is the bearing speed (rpm), v_0 is kinematic oil viscosity (centistokes) and f_0 is a lubrication factor which depends on type of bearing and lubrication.

Table 4. Values of *z* and *y*. Adapted with permission from [69], Taylor and Francis Group LLC, 2019.

Bearing Type	Nominal Contact Angle (Degrees)	z	y
Radial deep-groove	0	0.0004–0.0006	0.55
Thrust	90	0.0008	0.33
Double-row self-aligning	10	0.0003	0.4
Angular-contact	30–40	0.001	0.33

The power losses of the ball bearing can be simply defined in terms of the bearing torque and speed as presented in Equation (25) [71].

$$P_{bearing} = (t_l + t_v)\omega \tag{25}$$

Substituting the values of the parameters from Tables 2 and 3, Equation (25) can be simplified as:

$$P_{bearing} = 0.013\omega + 2.67 \times 10^{-4}\omega^{1.66} \tag{26}$$

3.3.3. Stray Losses

Stray losses are caused by the magnetic flux leakages of an electrical machine and can be categorised as the stator and rotor stray losses. Due to very little changes in the magnetic flux distribution of the IM stator from no load to full load, stray load losses in the stator of the IM can be neglected. Stray losses in the rotor of IM is a function of the frequency and depends on the rotor slip. In a squirrel cage induction machine (SCIM) with small slip, rotor stray losses are very small and can be neglected [72]. However, during normal operation where the IM operates at full or partial load, these losses cannot be neglected and can be estimated using Equation (27) as recommended by IEEE standards for calculating stray losses in electrical machines [73].

$$P_{stray} = 0.005 \frac{P_g^2}{P_r} \tag{27}$$

where P_g is the generated power or output power of the machine and P_r is the rated power.

4. Design and Control of SCIM-FESS

The general schematic of the model discussed in this paper is presented in Figure 3. The flywheel rotor coupled with the SCIM is modelled as an inertia added to the shaft of the SCIM. The dynamics of SCIM-flywheel can be analysed and represented by Equation (28).

$$J_0 \frac{d\omega}{dt} = T_e - B\omega \tag{28}$$

where T_e (N·m) is the electromechanical torque, ω (rad/s) is the angular velocity of the flywheel, J_0 is the combined inertia ($J_0 = J_{SCIM} + J_{flywheel}$) of the IM and flywheel rotor (kg·m^2) and B is the damping coefficient (N·m·s/rad).

The dynamic equations of the stator and rotor voltages of the SCIM are presented in Equations (29) and (30), respectively. For the ease of analysis and modelling of the control schemes, time varying sinusoidal quantities are transformed into *d-q* synchronous rotating frame by Park's transformation. A detailed analysis and description of the dynamic model of SCIM is discussed in [74].

$$
\begin{cases}
v_{ds} = R_s i_{ds} - \omega_e \lambda_{qs} + \frac{d}{dt}\lambda_{ds} \\
v_{qs} = R_s i_{qs} + \omega_e \lambda_{ds} + \frac{d}{dt}\lambda_{ds}
\end{cases}
\tag{29}
$$

$$
\begin{cases}
0 = R_r i_{dr} - (\omega_e - \omega_r)\lambda_{qr} + \frac{d}{dt}\lambda_{dr} \\
0 = R_r i_{qr} + (\omega_e - \omega_r)\lambda_{dr} + \frac{d}{dt}\lambda_{qr}
\end{cases}
\tag{30}
$$

where, R_r and R_s are rotor and stator resistances (ohms), v_{dqs} is the stator voltage in *d-q* reference frame (V), λ_{dqr} and λ_{dqs} are rotor and stator magnetic flux linkages in *d-q* reference frame (Wb), i_{dqr} and i_{dqs} are rotor and stator currents in *d-q* reference frame (A), and ω_e is the stator electrical speed (rad/s).
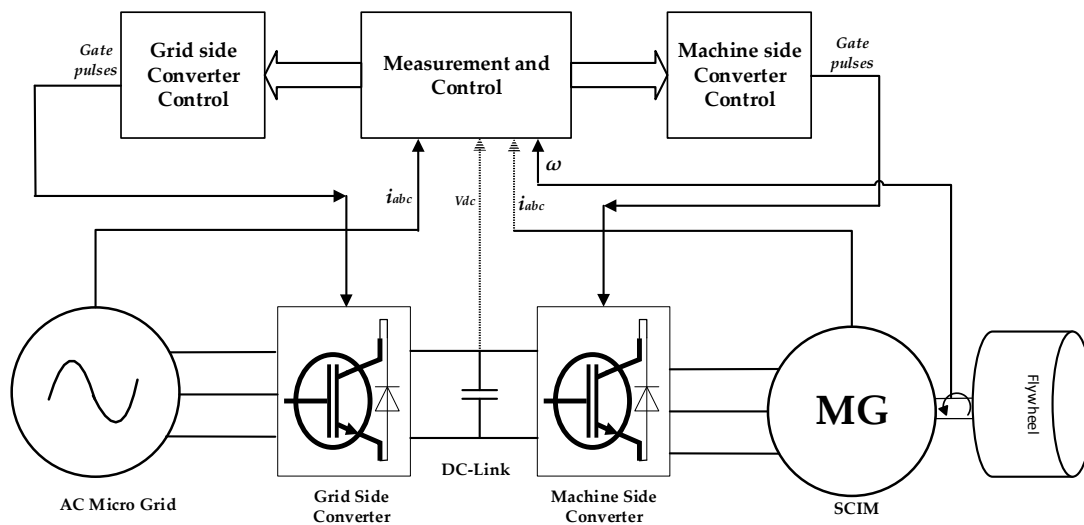

**Figure 3.** Schematic diagram of FESS.

The three-phase currents and the power flow from the electric grid are controlled by a vector-controlled grid side converter (GSC). The GSC acts as a rectifier or an inverter during acceleration and deceleration modes, respectively. Also, it regulates the DC-link voltage and the reactive currents exchanged with the electric grid. The speed and position of the flywheel are controlled by the machine side converter (MSC) that is connected to the GSC through a DC-link capacitor.

The three-phase currents of the machine and grid, the DC-link voltage and the position and speed of flywheel shaft are measured quantities, which are inputs to the measurement and control block. The control block calculates the position of the shaft and compares the measured quantities with reference values to generate the gates pulses for GSC and MSC. During acceleration mode of the flywheel when power is consumed from the electric grid, the GSC acts as a rectifier and MSC acts as an inverter. When the flywheel reaches its reference speed value, no energy conversion occurs and it switches to standby mode, during which, the flywheel runs at an optimum speed except for the marginal speed decrease due to standby losses. In contrast, when a disturbance occurs in an electric grid, the flywheel starts to decelerate (discharge), the GSC acts as an inverter and MSC operates as a rectifier.

4.1. Control Structure of SCIM-FESS

Important quantities to be controlled in a FESS are the DC-link voltage (V_{dc}), electromagnetic torque (T_e), speed (ω_m) and position of the rotor magnetic flux vector (θ_e) during acceleration and deceleration of the flywheel when operating within a specified range of speed. Field oriented control

(FOC) and space vector pulse width modulation (SVPWM) have been utilised to control the gate pulses of MSC and GSC. Figure 4 shows a detailed control structure of both converters.
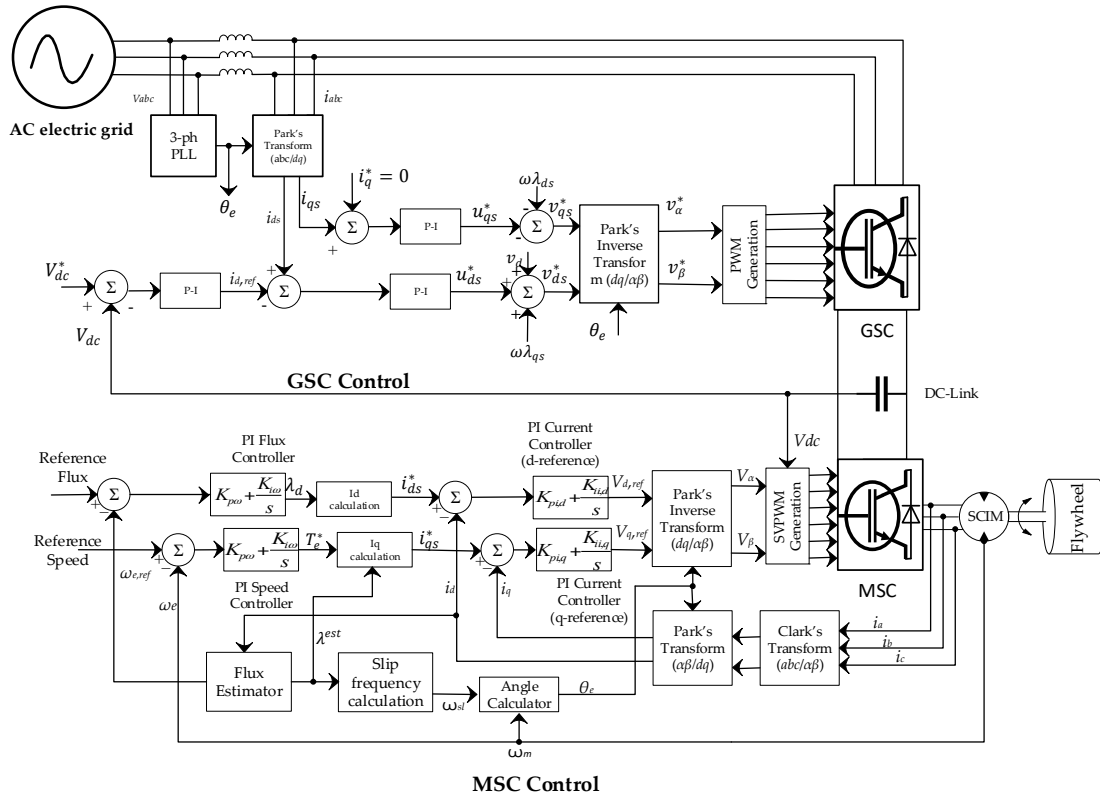
Figure 4. Control structure of machine side converter (MSC) and grid side converter (GSC) in squirrel-cage induction machine-based flywheel storage system (SCIM-FESS).

4.1.1. Machine Side Converter Control

The FOC controls the torque producing current (*iq*) and magnetic flux producing current (*id*) separately leading to a simple control structure as of a DC machine with less uncertainty of parameter variations [75]. As shown in Figure 4, the feedback loop is formed by measuring three-phase stator currents, which are then transformed into the synchronous *d-q* reference frame by Park's transformation. DC stator currents i_{ds} and i_{qs} are compared with reference currents i_{ds}^* and i_{qs}^* using PI current controllers which will produce reference voltage signals v_{ds}^* and v_{qs}^* for generating gate pulses for MSC by SVPWM modulator. Flux estimator calculates the actual magnitude of rotor magnetic flux using Equation (31) which is then compared with the reference flux. Reference d-q axis currents i_{ds}^* and i_{qs}^* are calculated using Equations (32) and (33) respectively by currents (*i_d and i_q*) calculator blocks. Calculated reference values of stator currents in synchronous *d-q* reference frame are compared with actual stator currents to produce reference voltages (V_{dref} and V_{qref}). The rotor flux angle is a crucial parameter in this control technique and it is used to determine the position of rotor flux in IM as calculated using Equations (34) and (35).

$$\lambda^{est} = \frac{L_m i_d}{1 + sT_r} \tag{31}$$

$$i_{ds}^* = \frac{\lambda_d}{L_m} \tag{32}$$

$$i_{qs}^* = \frac{2}{3} \cdot \frac{2}{P} \cdot \frac{L_r}{L_m} \cdot \frac{T_e^*}{\lambda^{est}} \tag{33}$$

$$\theta_e = \int (\omega_m + \omega_{sl}) dt \tag{34}$$

$$\omega_{sl} = \frac{i_{qs}^*}{i_{ds}^*} \cdot \frac{1}{T_r} \tag{35}$$

where λ^{est} is an estimated flux, λ_d is d-axis rotor magnetic flux linkage, T_e^* is the reference electromagnetic torque produced by PI controller, L_m and L_r is mutual inductance and rotor inductance respectively, ω_{sl} is the slip frequency, T_r is the rotor time constant, i_{ds}^* and i_{qs}^* are the reference stator currents.

4.1.2. Grid Side Converter Control

A direct vector control scheme is used to control i_d and i_q in order to regulate the DC-link voltage during the charge, discharge and standby modes of the flywheel (Figure 4). Input variables to the controller are three phase currents (i_{abc}), three-phase voltages (v_{abc}), grid frequency (ω) at the point of grid connection and DC-link voltage (V_{dc}). The reference input variables to the controller are reference DC-link voltage (V_{dc}^*) and d-axis reference current (i_{ds}^*), which is produced by a DC voltage regulator. The compensator term ($\omega\lambda_{dqs} = \omega L_g i_{dqs}$) eliminates coupling between d-q axis components and also reduces the error in the reference voltage (v_{ds}^*) produced by P-I regulator in order to accurately produce command voltage for modulation and generation of gating signals for switching devices. Using reference voltages, (v_{ds}^* *and* v_{ds}^*) the controller produces the set point values of voltages in the stationary reference frame ($v_{\alpha\beta}^*$) at the terminals of the IGBT voltage source converter to produce PWM switching pulses at the desired frequency. For simplification of control system d-axis component of two-phase system is oriented to the direction of grid voltage vector, therefore the grid side voltage (v_s) is equal to d-axis voltage (v_d) of two phase coordinate frame ($v_s = v_d$) and q-axis component is gained as $v_q = 0$ [76]. The angle for transforming three-phase currents (i_{abc}) into d-q reference frame is provided by phase locked loop (PLL) at grid frequency. The control strategy of the GSC is shown in Figure 4 and is governed by Equations (36) [77].

$$\left. \begin{array}{l} L_g \frac{di_{ds}}{dt} = -R_g i_{ds} + \omega\lambda_{qs} + v_s - v_{ds}^* \\ L_g \frac{di_{qs}}{dt} = -R_d i_{qs} - \omega\lambda_{ds} - v_{qs}^* \end{array} \right\} \tag{36}$$

where L_g and R_g are grid side inductance and resistance, v_s is grid side voltage. In this control strategy, a unity power factor is assumed, therefore, $i_q = 0$ and $i_{d,ref}$ are generated by a PI controller by comparing the reference and measured dc voltage (V_{dc}).

5. Results and Analysis

In reference to the dynamic equations and control structure presented in the above sections, the model of SCIM-FESS is developed in MATLAB/Simulink environment as shown in Figure 5. The mathematical relations developed for mechanical and electrical losses as well as the power electronics losses are also embedded in the model to account for the system losses. The SCIM-FESS is set to run for 20 min and dynamic analysis is performed during acceleration and deceleration states within a speed range of 10–20 krpm. During the acceleration state, a positive torque of 90 N·m is applied to charge the flywheel. During the deceleration mode, a negative torque of 90 N·m is applied where the flywheel delivers energy to the electric grid. The SCIM-FESS is designed to deliver 5 kWh of useable energy during which the DC-link voltage is set to 600 V and maintained by the GSC and MSC during different states of operation.
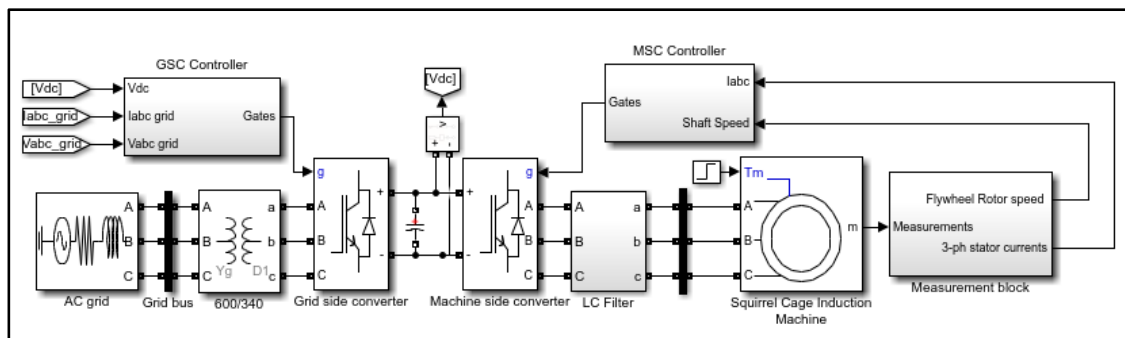
Figure 5. MATLAB/Simulink model of SCIM-FESS.

5.1. Acceleration Mode

The flywheel starts to accelerate when a positive torque of 90 N·m is applied and is fully charged in approximately 2.17 min. Then, at $t = 130.2$ s, the flywheel transfers to standby mode in 0.06 s when the mechanical torque and stator currents drop to zero—Allowing the flywheel to run idle with a stored energy of 5 kWh. Figure 6 presents the results of energy storage and percentage state of charge (% SoC) of the flywheel. During the transition from charging to standby mode, three-phase currents reduce to zero smoothly with no major current spikes or waveform distortions as shown in Figure 7. The system is left on standby mode for a long period of time ($t = 130.2$–1200 s) to show the flywheel fast charging and idling losses.
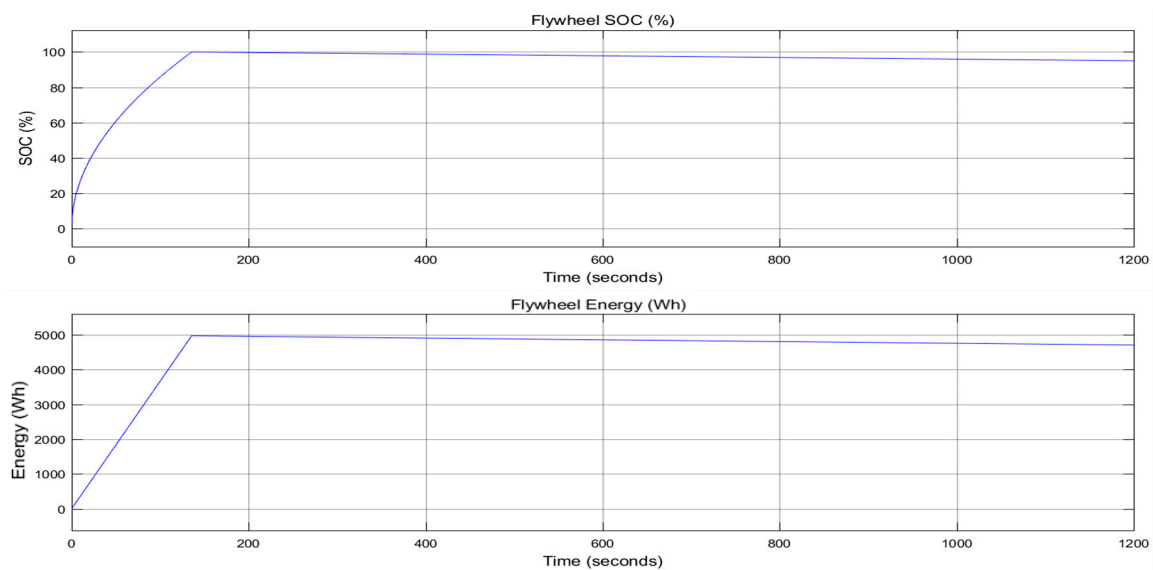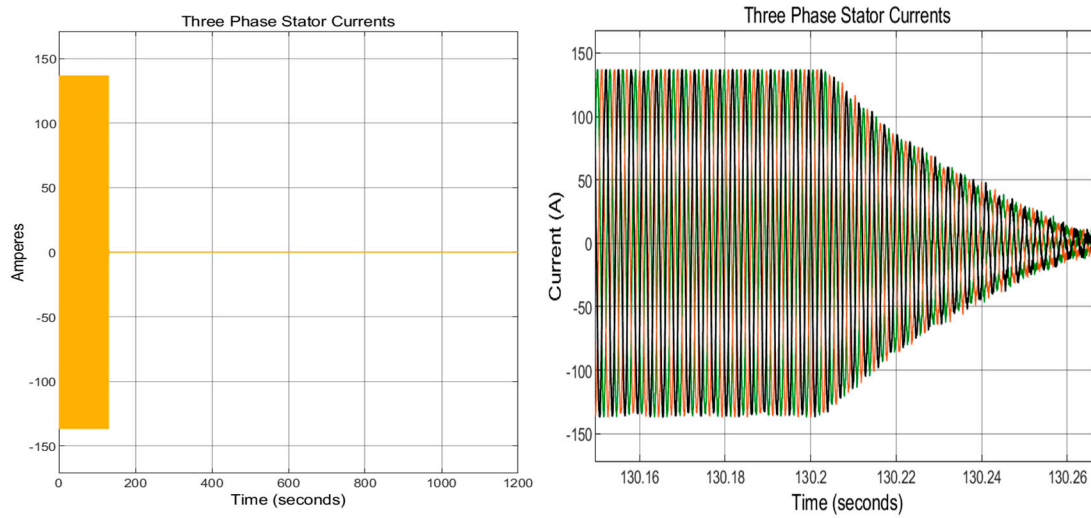

**Figure 6.** %SoC and energy stored by flywheel.

Figure 7. Three phase stator currents of IM during acceleration and standby mode.

During the standby mode, the flywheel speed and SoC are decreased due to the system losses including the aerodynamic and bearing friction losses. The copper losses are zero because currents stop flowing in the stator of the IM during the standby mode due to the use of electromagnets in the stator windings. During the standby mode, the flywheel state of charge drops to 96.5% due to self-discharge giving about 215 Wh of energy losses which is 4.3% of the total stored energy. Total power loss (p.u.) in standby mode is calculated by ratio between change in kinetic energy of the flywheel $\left(\Delta KE_{flywheel}\right)$ in Joules over the period of (Δt) in second, with respect to the rated kinetic energy of the flywheel ($KE_{rated\ FESS}$) in Joules, as expressed by Equation (37) [78]. Calculation of power loss gives 9.5% of total power lost over the period of 20 min.

$$\%P_{loss} = \frac{(\Delta KE_{FESS})}{\Delta t \times KE_{rated\ FESS}} \times 100 \tag{37}$$

5.2. Deceleration-Acceleration Mode at Constant Torque

To analyse the flywheel performance during acceleration and deceleration states, different charge-discharge operations are performed during the period of 20 min. A constant torque operation is performed here to show the system responsiveness due to step torque variations that can be accounted for the load variations in real life situations. Therefore, the flywheel is initially charged for 130.2 s, then switched to standby mode for 300 s before starting to discharge due to a negative torque of 90 N·m applied at $t = 430$ s (Figure 8). In order to test the dynamic stability of the SCIM-FESS model, multiple operations where performed by accelerating and decelerating the flywheel. At $t = 530$ s, the flywheel starts charging for 100 seconds before the charging torque is reversed to decelerate the flywheel at $t = 630$ s. Then the flywheel goes into the standby mode ($t = 720$ s) and spins with 22% of SoC and 0.4 kWh of stored energy. Different charging and discharging states of the flywheel and corresponding three-phase currents and torque waveforms are shown in Figure 8. Magnified images of three-phase stator currents and torque are shown in Figure 9 where it can be seen that IM smoothly switches from generating to motoring mode in less than 5 m s without any spikes or transients in the current waveforms showing the compliance and better performance of the machine side control system (MSC).
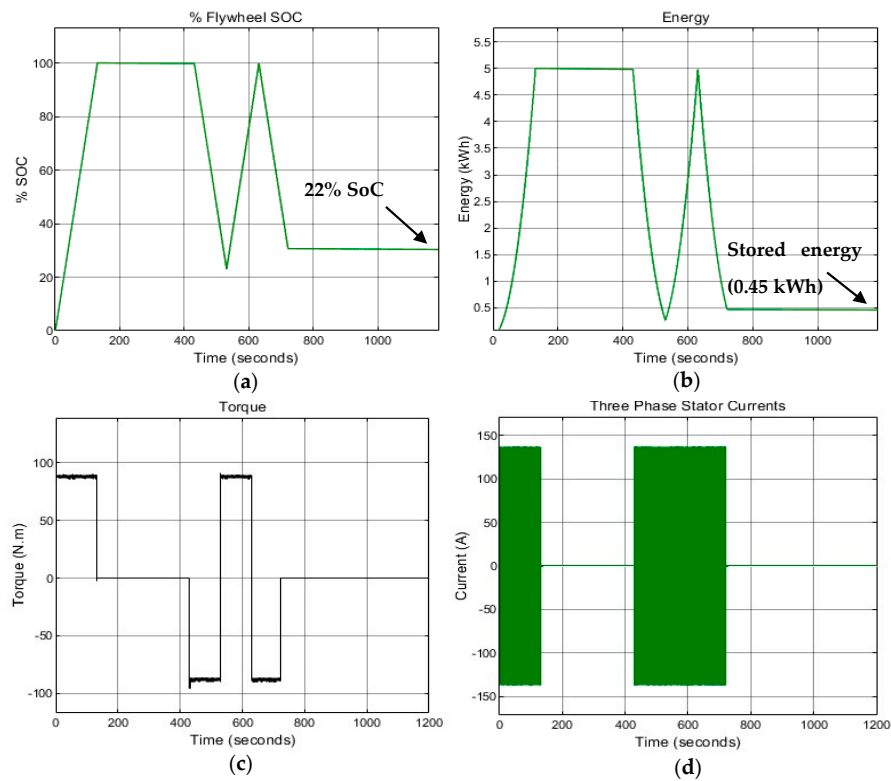
Figure 8. SCIM-FESS acceleration-deceleration mode: (**a**) %SoC of the flywheel; (**b**) Energy stored; (**c**) Mechanical torque; (**d**) Three phase stator currents.
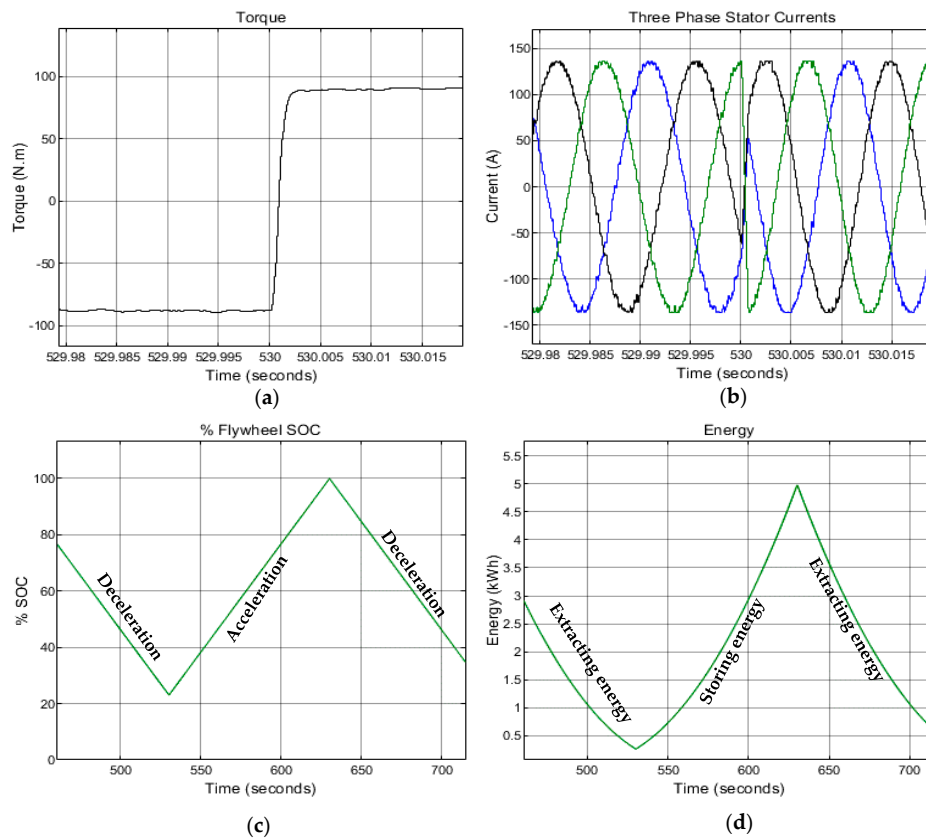
Figure 9. (**a**) Torque at *t* = 530 s; (**b**) Magnified three phase currents; (**c**) %SoC at *t* = 530 s; (**d**) stored energy in kWh.

5.3. Deceleration-Acceleration Mode at Variable Torque

In this section the model is simulated to run at different values of torque (variable torque) for a real-life application such as transport or during variable loads on the electric grid. The flywheel is initially charged by a positive torque (90 N·m) for 50 s and then the torque is reduced to 70 N·m where the flywheel speed is reduced and the charging rate is slowed down as shown in Figure 10. At t = 80 s the torque is further reduced to 50 N·m and the flywheel charges slower than before with reduced three-phase currents. It can be seen from Figures 10 and 11 that SCIM-FESS operates stably under different load conditions and the three-phase currents and speed of the flywheel comply with the torque variations during acceleration and deceleration modes.
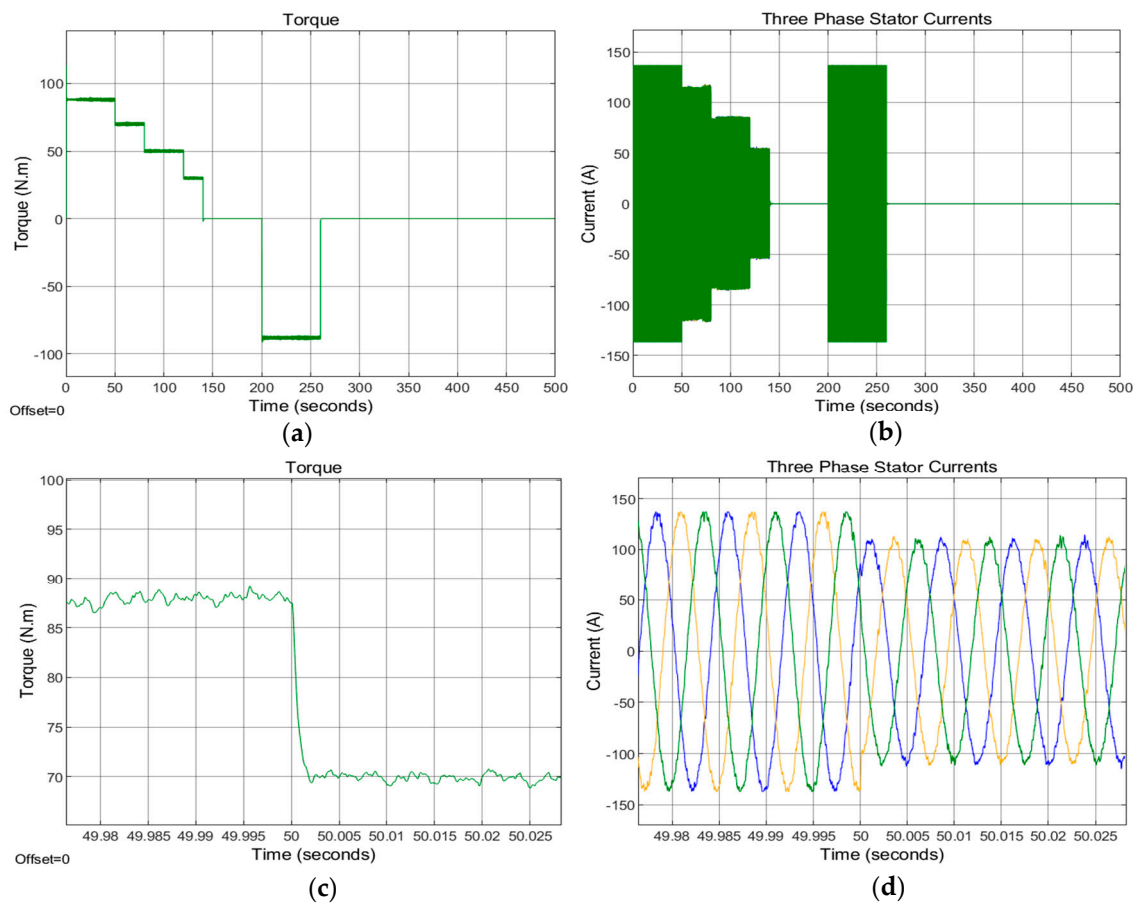

Figure 10. (**a**) Variable torque values; (**b**) Three phase currents at variable toque values; (**c**) Magnified view of change in torque command; (**d**) Magnified view of currents at t = 50 s.

Figure 12 shows DC-link voltage at a reference value of 600 V during acceleration and deceleration at different torque values. It can be seen that voltage remains stable at a reference value of 600 V and varies ±2 V from the reference value as shown in a magnified view in Figure 12. Better regulation and stability of DC voltage under different load conditions (torques values) exhibits the better performance of the GSC controller as discussed in Section 4.1.2.
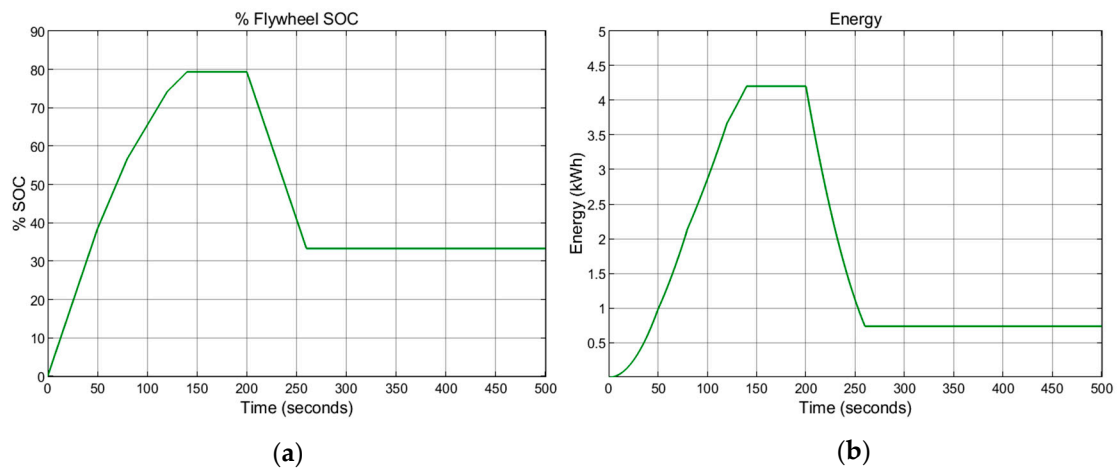
Figure 11. (**a**) % SoC of the flywheel at different torque; (**b**) Energy stored in the flywheel at different times.
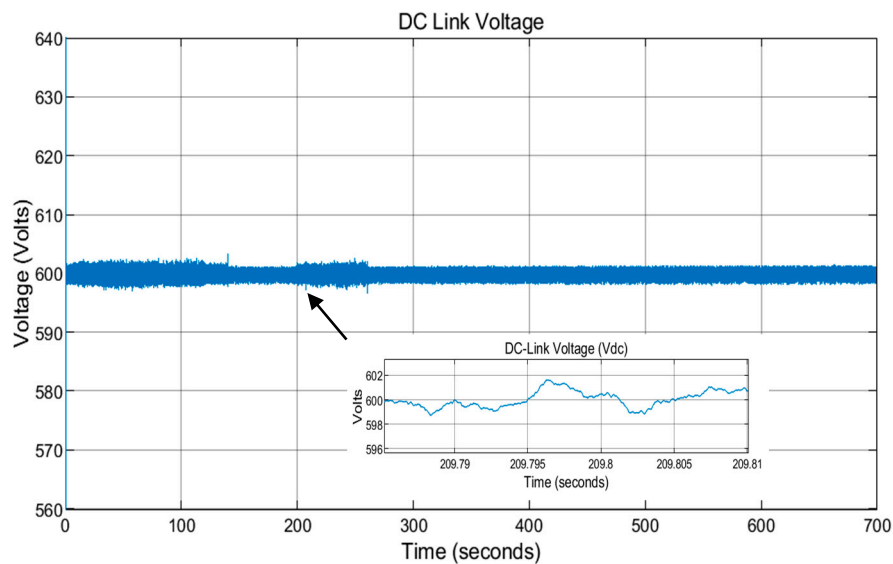
Figure 12. DC-link voltage during different states of operation and variable torque values.

5.4. SCIM-FESS Losses

The mechanical losses of the FESS are calculated based on the derived equations and the methods described in Section 3. The stray losses (eddy current and core losses) as well as the bearing and windage losses of the flywheel system as a function of the rotational speed is shown in Figure 13. Since the bearing loss is a function of the speed and the load on the bearing, and the windage loss is dependent on the speed and pressure of the flywheel rotor containment, these losses are lower in comparison to the stray losses (nearly 1.8 kW at 20,000) and are not related to the power rating of the motor/generator. For the maximum rated speed of 20,000 rpm, the bearing friction loss is approximated as 110 W and the windage loss at the atmosphere pressure level is about 90 W, giving a total of 200 W for combined windage and bearing losses. However, the system losses need to be kept at a minimum and particularly the standby losses, which is directly affected by the aerodynamic and bearing losses. Therefore, if the pressure level is kept below 10 Pa and the speed is maintained at 20,000 rpm, the windage losses will be 60% reduced as compared to the case of atmospheric pressure (Figure 13c).
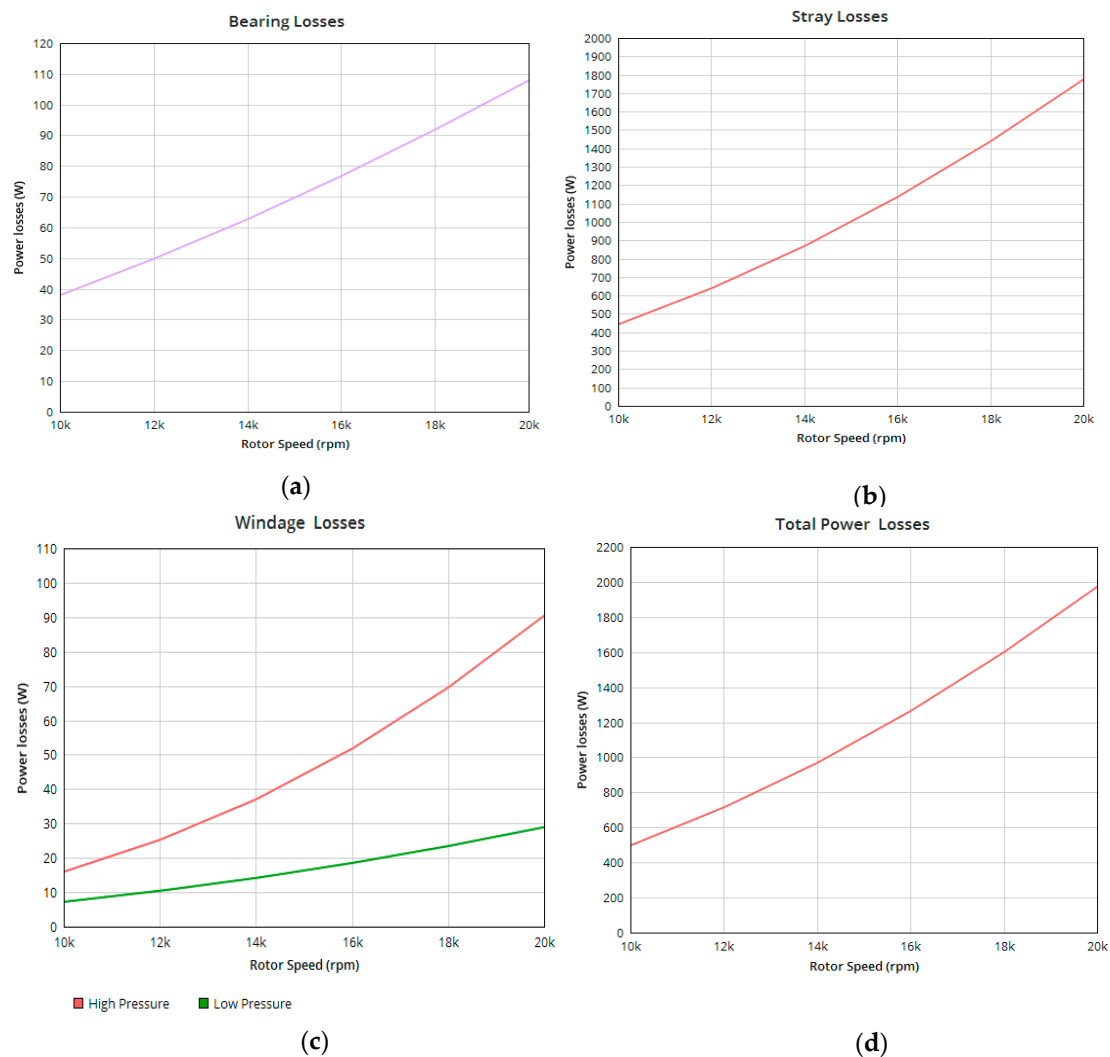
Figure 13. Different mechanical losses of SCIM-FESS: (**a**) Bearing losses due to load and speed torque; (**b**) Stray losses due to magnetic flux leakages; (**c**) Windage losses at low and high pressures;(**d**) Total mechanical losses.
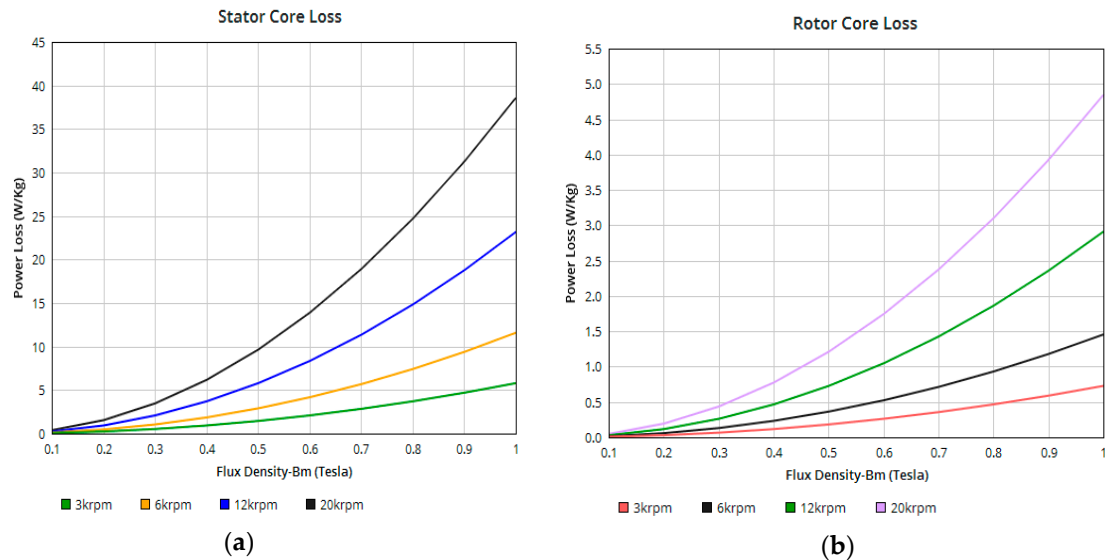
Stator and rotor specific core losses of SCIM-FESS are shown in Figure 14. The core losses occur in largest fraction in the stator of the IM because at low slip, the IM operates at nearly synchronous speed and the relative speed of magnetic fields over the rotor surface are slow, therefore, rotor core losses are very small compared to stator core losses [79].

As shown in Figure 14a, the specific core losses increase exponentially with increase in speed and magnetic flux density. The stator specific core losses are not significant for values of magnetic flux density up to 1 Tesla and 3 krpm speed. However, the specific core losses in stator of IM increase significantly above 3 krpms and even at 0.648 Tesla, the power losses due to hysteresis and eddy currents in stator core of IM operating at 20 krpm is 16.48 W/kg. Rotor specific core losses of IM are shown in Figure 14b and it can be seen that rotor specific core losses increases exponentially with increase in maximum magnetic flux density. However, even at a high speed of 20 krpm, the rotor specific core losses are not significant.

The copper loss in the IM is directly proportional to square of the current and is a function of current and resistance. Copper losses in the stator and rotor of the IM are measured by simulating the copper loss models (Equations (16) and (17)) in MATLAB/Simulink software. The SCIM-FESS dynamic performance was analysed at different torque magnitudes in order to demonstrate copper losses at different values of three phase currents. The system was operated with initial positive torque of 50 N·m

for 50 s in charging mode and then the torque was increased to its maximum rated value of 90 N·m for 30 s. When the flywheel was at standby mode (*t* = 80 s), there were no currents flowing through the rotor and stator windings of the IM as shown in Figure 15a,b. At *t* = 100 s, the IM operated as a generator and flywheel started discharging for 20 s until switching back to standby mode at *t* = 120 s.

Figure 14. Specific core losses of SCIM-FESS: (**a**) Stator core losses; (**b**) Rotor core losses.
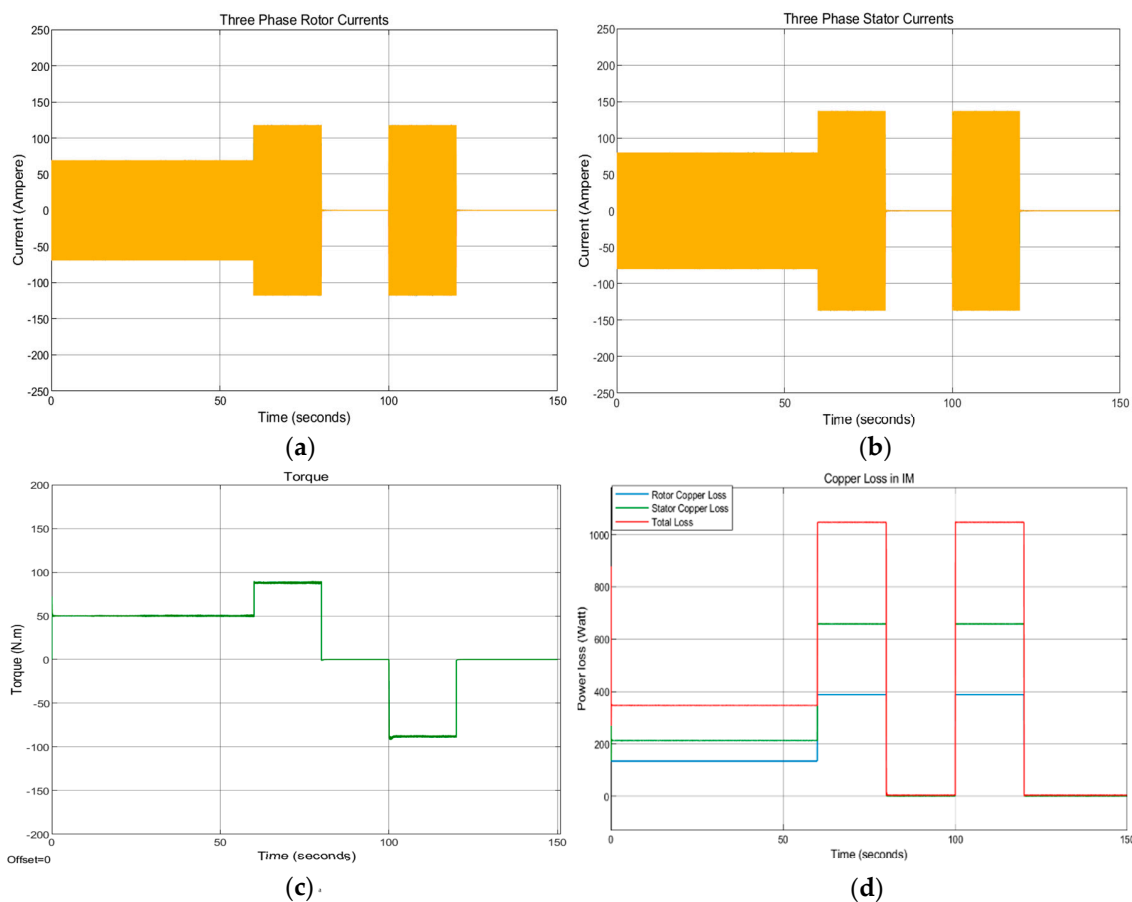
Figure 15. (**a**) Three phase rotor currents; (**b**) Three phase stator currents; (**c**) Torque commands; (**d**) Copper losses in rotor and stator of IM.

The rotor and stator copper losses vary with currents as torque is varied on the shaft of the IM (Figure 15c). Stator copper losses at maximum three-phase current is 657 Watts and it decreases to zero when torque from the shaft of IM is removed. Rotor copper losses at maximum three-phase rotor current is 388 Watts and the combined total copper losses of the IM at maximum three-phase current and maximum operating torque is 1.045 kW.

As a comparison to the loss model of the SCIM-FESS presented in this research, the performance analysis of a PMSM-FESS for the same system rating (100 kW, 5 kWh and 10–20 krpm) is presented in reference [29]. It is shown that the IM draws high inrush current at the starting but operates normally during the transition periods between charge-discharge states. For the case of PMSM, it starts normally with no major inrush currents but has higher standby losses. In contrary, IM do not use permanent magnets and has not standby electrical losses.

6. Discussion and Conclusions

This paper presented the analysis of the dynamic performance of a squirrel-cage induction machine integrated to a flywheel storage with a developed model in MATLAB/Simulink. The structure of the control system as well as the comprehensive loss model consisted of the electrical, mechanical and power electronics losses were also discussed and embedded in the model. A detailed simulation model of a 100 kW IM drive was presented and analysed in different states of charging, discharging and standby modes.

The presented results show the analysis of an induction machine driven flywheel storage system during different modes of operation including constant and variable torque conditions. The dynamic performance of the system was analysed for the two general cases of constant power and constant torque operations and the results of the analysis were presented. The SCIM-FESS was operated within a speed range of 10–20 krpm at a shaft torque of 90 N·m storing 5 kWh of energy in 2.17 min. The presented system with the proposed control system and parameters of the machine, can store more energy at higher speed (more than 20 krpm) at the expense of higher windage losses. When the torque on the flywheel is zero during standby mode, an energy loss of 215 Wh occurs in a period of approximately 18 min where the flywheel speed reduces to 19,480 rpm due to the windage effect and frictional component of the bearing torque. The standby losses of the system can be reduced by maintaining a low vacuum and using a better technology for the bearing system such as magnetic bearing but this will increase the cost of the system. Aerodynamic drag of the rotor can be reduced by housing the rotor in low a vacuum chamber, and can reduce the losses considerably as shown in Figure 13. Copper and iron losses in the stator of IM are negligible during standby mode as no currents flow in the stator of the IM (Figure 15) and, therefore, no magnetic field exists due to use of electromagnets in the stator windings. This is a significant advantage of IM over PMSM as it reduces total losses of the system providing better efficiency.

Stable operation of the system implies that the use of the proposed control system in IM drive provides better performance and quick reversal electromagnetic torque during the transition from generating to motoring mode and vice versa. Operation scenarios of FESS presented in Sections 5.2 and 5.3 are the benchmarks for flywheel applications in transport and in an electric grid under different load conditions. The presented results show a realistic system with drag losses working stably in different conditions which justifies the proper working of control systems proposed in the paper. Also, the SCIM-FESS can be explored and analysed for use with a renewable energy source and a diesel generator set which can be used for energy management and ride through applications. This can improve the efficiency of the intermittent renewable energy source and save fuel costs of the associated diesel generator set.

The results of the analysis show that the SCIM-FESS has satisfactory characteristics in energy regulation and dynamic response during load torque variations. SCIM drive system makes use of the vector control technique to control power electronics converters in order to follow the reference value commands of torque, speed and voltage. The machine side field-oriented control system provides

quick reversal of magnetic field at the time when torque is reversed and the IM switches from generator to motor mode in less than 5 ms (Figure 9b). This can be a benefit in applications requiring fast response and involving critical loads such as in data centers. The vector controller of grid converter maintains a constant dc voltage during different load scenarios, which helps to improve the stability at the point of connection when the flywheel is integrated with renewable sources in an electric grid. Further research on this model will focus on making use of a SCIM-FESS in electric grid incorporating wind energy system.

Author Contributions: Conceptualization, A.S. and M.E.A.; Formal Analysis, D.N.; Writing-Original Draft Preparation, A.S.; Writing-Review & Editing, M.E.A. and K.R.P.; Supervision, K.R.P.

References

1. Hadjipaschalis, I.; Poullikkas, A.; Efthimiou, V. Overview of current and future energy storage technologies for electric power applications. *Renew. Sustain. Energy Rev.* **2009**, *13*, 1513–1522. [CrossRef]
2. Guney, M.S.; Tepe, Y. Classification and assessment of energy storage systems. *Renew. Sustain. Energy Rev.* **2017**, *75*, 1187–1197. [CrossRef]
3. Amiryar, M.E.; Pullen, K.R.; Nankoo, D. Development of a High-Fidelity Model for an Electrically Driven Energy Storage Flywheel Suitable for Small Scale Residential Applications. *Appl. Sci.* **2018**, *8*, 453. [CrossRef]
4. Sabihuddin, S.; Kiprakis, A.E.; Markus, M. A Numerical and Graphical Review of Energy Storage Technologies. *Energies* **2015**, *8*, 172–216. [CrossRef]
5. Mohamad, F.; Teh, J.; Lai, C.-M.; Chen, L.-R. Development of Energy Storage Systems for Power Network Reliability: A Review. *Energies* **2018**, *11*, 2278. [CrossRef]
6. Breeze, P. An Introduction to Energy Storage Technologies. In *Power System Energy Storage Technologies*; Elsevier BV: Amsterdam, The Netherlands, 2018; pp. 1–11.
7. Hittinger, E.; Whitacre, J.; Apt, J. What properties of grid energy storage are most valuable? *J. Power Sources* **2012**, *206*, 436–449. [CrossRef]
8. Bender, D. Flywheels. In Proceedings of the Electrical Energy Storage Techniques, System Surety Engineering, Sandia National Laboratories, Livermore, CA, USA, 17 February 2016; pp. 183–201.
9. Thoolen, F. *Development of an Advanced High Speed Flywheel Energy Storage System Eindhoven*; Technische Universiteit Eindhoven: Eindhoven, The Netherlands, 1993.
10. Maass, D. Integral Composite Flywheel Rim and Hub. U.S. Patent No. 5,784,926, 28 July 1998.
11. Hedlund, M.; Kamf, T.; De Santiago, J.; Abrahamsson, J.; Bernhoff, H. Reluctance Machine for a Hollow Cylinder Flywheel. *Energies* **2017**, *10*, 316. [CrossRef]
12. Krack, M.; Secanell, M.; Mertiny, P. Rotor Design for High-Speed Flywheel Energy Storage Systems. In *Energy Storage in the Emerging Era of Smart Grids*; IntechOpen: London, UK, 2011; pp. 41–68.
13. Bolund, B.; Bernhoff, H.; Leijon, M. Flywheel energy and power storage systems. *Renew. Sustain. Energy Rev.* **2007**, *11*, 235–258. [CrossRef]
14. Arani, A.K.; Karami, H.; Gharehpetian, G.; Hejazi, M. Review of Flywheel Energy Storage Systems structures and applications in power systems and microgrids. *Renew. Sustain. Energy Rev.* **2017**, *69*, 9–18. [CrossRef]
15. Wicki, S.; Hansen, E.G. Clean energy storage technology in the making: An innovation systems perspective on flywheel energy storage. *J. Clean. Prod.* **2017**, *162*, 1118–1134. [CrossRef]
16. Ibrahim, H.; Ilinca, A.; Perron, J. Energy storage systems—Characteristics and comparisons. *Renew. Sustain. Energy Rev.* **2008**, *12*, 1221–1250. [CrossRef]
17. Arghandeh, R.; Pipattanasomporn, M.; Rahman, S. Flywheel Energy Storage Systems for Ride-through Applications in a Facility Microgrid. *IEEE Trans. Smart Grid* **2012**, *3*, 1955–1962. [CrossRef]
18. Schmidt, O.; Melchior, S.; Hawkes, A.; Staffell, I. Projecting the Future Levelized Cost of Electricity Storage Technologies. *Joule* **2019**, *3*, 81–100. [CrossRef]
19. Shuhei, K.; Miao-miao, C.; Hideo, S.; Ryuichi, S. Semiconductor Power Converterless Voltage Sag Compensator and UPS Using a Flywheel Induction Motor and an Engine Generator. In Proceedings of the Power Conversion Conference, Nagoya, Japan, 2–5 April 2007.

20. Kimura, N.; Sonoda, M.; Morizane, T.; Taniguchi, K.; Kurokawa, F. Emergency power supply using flywheel and doubly fed induction generator. In Proceedings of the 31st International Telecommunications Energy Conference (INTELEC), Incheon, Korea, 18–22 October 2009; pp. 1–6.

21. Lashway, C.R.; Elsayed, A.T.; Mohammed, O.A. DC voltage ripple quantification for a flywheel-battery based Hybrid Energy Storage System. In Proceedings of the IEEE Applied Power Electronics Conference and Exposition (APEC), Long Beach, CA, USA, 20–24 March 2016; pp. 1267–1272.

22. McGroarty, J.; Schmeller, J.; Hockney, R.; Polimeno, M. Flywheel energy storage system for electric start and an all-electric ship. In Proceedings of the IEEE Electric Ship Technologies Symposium, Philadelphia, PA, USA, 27 July 2005; pp. 400–406.

23. Zhao, B.; Zhang, X.; Chen, J. Integrated microgrid laboratory system. In Proceedings of the IEEE Power & Energy Society General Meeting, Vancouver, BC, Canada, 21–25 July 2013; p. 1.

24. Amiryar, M.E.; Pullen, K.R. Assessment of the Carbon and Cost Savings of a Combined Diesel Generator, Solar Photovoltaic, and Flywheel Energy Storage Islanded Grid System. *Energies* **2019**, *12*, 3356. [CrossRef]

25. Faraji, F.; Majazi, A.; Al-Haddad, K. A comprehensive review of Flywheel Energy Storage System technology. *Renew. Sustain. Energy Rev.* **2017**, *67*, 477–490.

26. Recheis, M.; Fulmek, P.; Wegleiter, H.; Schweighofer, B. Rotor Losses in a Switched Reluctance Motor—Analysis and Reduction Methods. *EPJ Web Conf.* **2013**, *40*, 17008.

27. Torrey, D. Switched reluctance generators and their control. *IEEE Trans. Ind. Electron.* **2002**, *49*, 3–14. [CrossRef]

28. Memon, A.A.; Shah, S.A.A.; Shah, W.; Baloch, M.H.; Kaloi, G.S.; Mirjat, N.H. A Flexible Mathematical Model for Dissimilar Operating Modes of a Switched Reluctance Machine. *IEEE Access* **2018**, *6*, 9643–9649. [CrossRef]

29. Soomro, A.; Amiryar, M.E.; Pullen, K.R.; Nankoo, D. Comparison of performance and controlling schemes of synchronous and induction machines used in flywheel enregy storage systems. *Energy Procedia* **2018**, *151*, 100–110. [CrossRef]

30. Amodeo, S.J.; León, A.E.; Chiacchiarini, H.G.; Solsona, J.A.; Busada, C.A. Non linear Control Strategies of a Flywheel driven by a Synchronous Homopolar Machine. In Proceedings of the IEEE International Symposium on Industrial Electronics, Vigo, Spain, 4–7 June 2007.

31. Severson, E.; Nilssen, R.; Undeland, T.; Mohan, N. Magnetic Equivalent Circuit Modeling of the AC Homopolar Machine for Flywheel Energy Storage. *IEEE Trans. Energy Convers.* **2015**, *30*, 1670–1678. [CrossRef]

32. Cárdenas, R.; Pena, R.; Asher, G.; Clare, J. Control strategies for enhanced power smoothing in wind energy systems using a flywheel driven by a vector-controlled induction machine. *IEEE Trans. Ind. Electron.* **2001**, *48*, 625–635. [CrossRef]

33. Cimuca, G.; Breban, S.; Radulescu, M.M.; Saudemont, C.; Robyns, B. Design and Control Strategies of an Induction-Machine-Based Flywheel Energy Storage System Associated to a Variable-Speed Wind Generator. *IEEE Trans. Energy Convers.* **2010**, *25*, 526–534. [CrossRef]

34. Kato, S.; Cheng, M.-M.; Sumitani, H.; Shimada, R. Flywheel size design considerations and experimental verification using a 50-kW system for voltage sag compensator with flywheel induction motor. *Electr. Eng. Jpn.* **2012**, *181*, 36–44. [CrossRef]

35. Kim, Y.-H.; Park, K.-S.; Jeong, Y.-S. Comparison of harmonic compensation based on wound/squirrel-cage rotor type induction motors with flywheel. In Proceedings of the Third International Power Electronics and Motion Control Conference (IPEMC), Beijing, China, 15–18 August 2000.

36. Zhang, J.; Chen, Z.; Cai, L.; Zhao, Y. Flywheel energy storage system design for distribution network. In Proceedings of the IEEE Power Engineering Society Winter Meeting, Singapore, 23–27 January 2000.

37. Cimuca, G.; Saudemont, C.; Robyns, B.; Radulescu, M. Control and Performance Evaluation of a Flywheel Energy-Storage System Associated to a Variable-Speed Wind Generator. *IEEE Trans. Ind. Electron.* **2006**, *53*, 1074–1085. [CrossRef]

38. Suzki, Y.; Koyanagi, A.; Kobarashi, M.; Shimada, R. Noverl applicaiton of the flywheel energy storage system. *Energy* **2005**, *30*, 2128–2143. [CrossRef]

39. Arani, A.A.K.; Zaker, B.; Gharehpetian, G.B. Induction machine-based flywheel energy storage system modeling and control for frequency regulation after micro-grid islanding. *Int. Trans. Electr. Energy Syst.* **2017**, *27*, e2356. [CrossRef]

40. Park, J.-D. Simple flywheel energy storage using squirrel-cage induction machine for DC bus microgrid systems. In Proceedings of the 36th Annual Conference on IEEE Industrial Electronics Society (IECON), Glendale, AZ, USA, 7–10 November 2010; pp. 3040–3045.

41. Kim, S.-H. *Electric Motor Control*; Elsevier Science: Amsterdam, The Netherlands, 2017.

42. Shelke, R.; Dighole, D. A Review paper on Dual Mass Flywheel system. *Int. J. Sci. Eng. Technol. Res.* **2016**, *5*, 326–331.

43. Aneke, M.; Wang, M. Energy storage technologies and real life applications—A state of the art review. *Appl. Energy* **2016**, *179*, 350–377. [CrossRef]

44. Hasan, N.S.; Hassan, M.Y.; Majid, M.S.; Rahman, H.A. Review of storage schemes for wind energy systems. *Renew. Sustain. Energy Rev.* **2013**, *21*, 237–247. [CrossRef]

45. Bitterly, J.G. Flywheel technology past, present, and 21st Century projections. *IEEE Aerosp. Electron. Syst. Mag.* **1998**, *13*, 13–18. [CrossRef]

46. Mears, L.; Gotschall, H.; Kamath, H.H. *EPRI-DOE Handbook of Energy Storage for Transmission and Distribution Applications*; Electric Power Research Insttute, Inc.: Palo Alto, CA, USA; U.S Department of Energy: Washington, DC, USA, 2003.

47. Sebastian, R.; Alzola, R.P. Flywheel energy storage systems: Review and simulation for an isolated wind power system. *Renew. Sustain. Energy Rev.* **2012**, *16*, 6803–6813. [CrossRef]

48. Truong, L.; Wolff, F.; Dravid, N. Simulation of flywheel electrical system for aerospace applications. In Proceedings of the 35th Intersociety Energy Conversion Engineering Conference and Exhibit, Las Vegas, NV, USA, 24–28 July 2000.

49. Kan, H.; Chau, K.; Cheng, K.M. Development of doubly salient permanent magnet motor flywheel energy storage for building integrated photovoltaic system. In Proceedings of the Sixteenth Annual IEEE Applied Power Electronics Conference and Exposition (APEC), Anaheim, CA, USA, 4–8 March 2001.

50. Reiner, G.; Wehlau, N. Concept of a 50 MW/650 MJ power source based on industry-established MDS flywheel units. In Proceedings of the 28th IEEE International Conference on Plasma Science and 13th IEEE International Pulsed Power Conference, Las Vegas, NV, USA, 17–22 June 2001.

51. Holm, S.R. Modelling and Optimization of Permanent Magnet Machine in a Flywheel. Ph.D. Thesis, Delf University of Technology, Delf, The Netherland, 2003.

52. Zhu, Z.Q.; Howe, D. Electrical Machines and Drives for Electric, Hybrid, and Fuel Cell Vehicles. *Proc. IEEE* **2007**, *95*, 746–765. [CrossRef]

53. Amiryar, M.E.; Pullen, K.R. A Review of Flywheel Energy Storage System Technologies and Their Applications. *Appl. Sci.* **2017**, *7*, 286. [CrossRef]

54. Liu, H.; Jiang, J. Flywheel energy storage—An upswing technology for Energy Sustainability. *Energy Build.* **2006**, *39*, 599–604. [CrossRef]

55. Sotelo, G.; De Andrade, R.; Ferreira, A. Magnetic Bearing Sets for a Flywheel System. *IEEE Trans. Appl. Supercond.* **2007**, *17*, 2150–2153. [CrossRef]

56. Ren, M.; Shen, Y.; Li, Z.; Nonami, K. Modeling and Control of a Flywheel Energy Storage System Using Active Magnetic Bearing for Vehicle. In Proceedings of the International Conference on Information Engineering and Computer Science, Wuhan, China, 19–20 December 2009; pp. 1–5.

57. Zhang, C.; Tseng, K.J. A Novel Flywheel Energy Storage System With Partially-Self-Bearing Flywheel-Rotor. *IEEE Trans. Energy Convers.* **2007**, *22*, 477–487. [CrossRef]

58. Qiu, Y.; Ding, H. Flywheel Energy Storage System with PermanentMagnetic Bearing and Spiral Groove Bearing. In Proceedings of the 8th International Conference on Mechanical and Intelligent Manufacturing Technologies, Cape Town, South Africa, 3–6 February 2017.

59. Ruddell, A. *Investigation on Storage Technologies for Intermittent Renewable Energies: Evaluation and Recommended R&D Strategy*; CCLRC-Rutherford Appleton Laboratory Chilton: Didcot, UK, 2003.

60. Alias, A.; Rahim, N.A.; Hussain, M.A. Bidirectional three phase power converter. In Proceedings of the IEEE Conference on Clean Energy and Technology (CET), Kuala Lumpur, Malaysia, 27–29 June 2011; pp. 337–341.

61. Oliveira, J.G.; Schettino, H.; Gama, V.; Carvalho, R.; Bernhoff, H. Implementation and Control of an AC/DC/AC Converter for Double Wound Flywheel Application. *Adv. Power Electron.* **2012**, *2012*, 604703. [CrossRef]

62. Elserougi, A.; Massoud, A.; Ahmed, S. Flywheel energy storage system based on boost DC-AC converter. In Proceedings of the IET Conference on Renewable Power Generation (RPG), Edinburgh, UK, 6–8 September 2011; p. 241.

63. Babuska, V.; Beatty, S.M.; deBlonk, B.J.; Fausz, J.L. A Review of Technology Developments in Flywheel Attitude Control and Energy Transmission Systems. In Proceedings of the IEEE Aerospace Conference Proceedings, Big Sky, MT, USA, 6–13 March 2004.

64. Popescu, M.; McGilp, M.I.; Miller, T.J.E.; Dellinger, S.J.; Heideman, R.J.; Ionel, D.M. Computation of Core Losses in Electrical Machines Using Improved Models for Laminated Steel. *IEEE Trans. Ind. Appl.* **2007**, *43*, 1554–1564.

65. Roy, R.; Prabhakar, K.K.; Kumar, P. Core-loss calculation in different parts of Induction Machine. *IET Electr. Power Appl.* **2017**, *11*, 11. [CrossRef]

66. Cogent Power Inc. Typical data for SURA® M470-50HP. Cogent Power. Available online: https://cogent-power.com/cms-data/downloads/m470-50hp.pdf (accessed on 30 July 2019).

67. Pyrhnen, J.; Jokinen, T.; Hrabovcov, V. *Design of Rotating Electrical Machines*; Wiley: Chichester, UK, 2008.

68. Liu, H.-P.; Werst, M.; Hahne, J.J.; Bogard, D. Prediction of Windage Losses of an Enclosed High Speed Composite Rotor in Low Air Pressure Environments. *Heat Transf.* **2003**, *1*, 15–23.

69. Harris, T.A.; Kotzalas, M.N. *Rolling Bearing Analysis*; Taylor & Francis Group LLC: Boca Raton, FL, USA, 2007.

70. Tu, M. Validation and Modeling of Power Losses of NJ 406 Cylindrical Roller Bearings. Master's Thesis, KTH Industrial Engineering and Management, Stockholm, Sweden, 2016.

71. SKF. Bearing Friction, Power Loss and Starting Torque. Available online: https://www.skf.com/uk/products/bearings-units-housings/principles/bearing-selection-process/operating-temperature-and-speed/friction-powerloss-startingtorque/index.html (accessed on 2 April 2019).

72. Davis, R.W. Notes on Induction Motor Losses. *Am. Inst. Electr. Eng.* **1913**, *32*, 363–367. [CrossRef]

73. Tamura, J. Calculation Method of Losses and Efficiency of Wind Generators. In *Waste Energy for Life Cycle Assessment*; Springer Science and Business Media LLC: Berlin/Heidelberg, Germany, 2012; pp. 25–51.

74. Feng, J.; Gongbao, W.; Lijun, F.; Yaqiao, Y.; Ruitian, W.; Zhen, X. Controller design of flywheel energy storage systems in microgrid. In Proceedings of the 17th International Conference on Electrical Machines and Systems (ICEMS), Hangzhou, China, 22–25 October 2014; pp. 2821–2826.

75. Amezquita-Brooks, L.; Liceaga-Castro, J.; Liceaga-Castro, E. Speed and Position Controllers Using Indirect Field-Oriented Control: A classical Control Approach. *IEEE Trans. Ind. Electron.* **2014**, *61*, 1928–1943. [CrossRef]

76. Sun, H.; Ren, Y.; Li, H.; An, Z.; Liu, J.; Hu, H.; Liu, H. DFIG wind power generation based on back-to-back PWM converter. In Proceedings of the International Conference on Mechatronics and Automation, Changchun, China, 9–12 August 2009; pp. 2276–2280.

77. Diaz-Gonzalez, F.; Sumper, A.; Gomis-Bellmunt, O. *Energy Storage in Power Systems*; John Wiley & Sons Ltd.: Chichester, UK, 2016.

78. Sheng, X. Design and Prototyping of a Low-Speed Flywheel System for Automotive Brake Energy Recovery. Undergraduate Honors Thesis, The Ohio State University, Columbus, OH, USA, 2012.

79. Chapman, S.J. *Elecrical Machinery Fundamentals*; McGraw-Hill Inc.: New York, NY, USA, 1991.